

The effect of melt pond geometry on the distribution of solar energy under first-year sea ice

C. Horvat¹, D. Flocco^{2,3}, D. W. Rees Jones^{4,5}, L. Roach^{6,7}, K. M. Golden⁸

¹Institute at Brown for Environmental Science, Brown University, Providence, RI, USA

²National Center for Atmospheric Science, Reading, UK

²Centre for Polar Observation and Modelling, Department of Meteorology, University of Reading,
Reading, UK

³Department of Earth Sciences, University of Oxford, Oxford, UK

⁴Bullard Laboratories, Department of Earth Sciences, University of Cambridge, Cambridge, UK

⁵National Climate Centre, National Institute of Water and Atmospheric Research, Wellington, NZ

⁶School of Geography, Environment & Earth Sciences, Victoria University of Wellington, Wellington, NZ

⁷Department of Mathematics, University of Utah, Salt Lake City, UT, USA

Key Points:

- The geometry of surface melt ponds affects the spatial heterogeneity of solar irradiance under sea ice.
- We define a metric to capture statistics of the sub-ice light field as a function of pond geometry.
- We explore the impact of changing surface geometry on under-ice primary production and sea-ice melting.

Corresponding author: Chris Horvat, horvat@brown.edu

Abstract

Sea ice plays a critical role in the climate system through its albedo, which constrains light transmission into the upper ocean. In spring and summer, light transmission through sea ice is influenced by its iconic blue melt ponds, which significantly reduce surface albedo. We show that the geometry of surface melt ponds plays an important role in the partitioning of solar radiation under sea ice by modeling the three-dimensional light field under ponded sea ice. We find that aggregate properties of the sub-ice light field, such as the enhancement of available solar energy under bare ice regions, can be described using a new parameter closely related to pond fractal geometry. We then explore the influence of pond geometry on the ecological and thermodynamic sea-ice processes that depend on solar radiation.

1 Introduction

Solar radiation is a major source of energy in polar regions and is the main driver of growth and melting of sea ice in the Arctic ocean (Perovich & Richter-Menge, 2009). The Arctic sea ice cover is heterogeneous, a mosaic of individual floes that range in size from meters to tens of kilometers. The emergent properties of small-scale sea ice surface variability, in particular the sea ice albedo, are important components of large scale numerical climate models.

At the beginning of the melt season, sea ice consists of a semi-permeable layer of ice covered by a comparatively thin layer of snow. As the snow layer melts, fresh melt water percolates into the upper ice layer and freezes (Polashenski et al., 2017). Subsequent melt water collects in topographic lows of the ice surface, forming small melt ponds (Polashenski, Perovich, & Courville, 2012). Over the course of the melt season, the ponds enlarge and merge, and constitute a significant fraction of the Arctic sea ice surface, particularly for first-year sea ice (Fetterer & Untersteiner, 1998; Rösel, Kaleschke, & Birnbaum, 2012). Their geometry becomes more complex, with a transition in fractal dimension as pond area grows (Hohenegger, Alali, Steffen, Perovich, & Golden, 2012).

Because of the high albedo of bare sea ice, changes to the sea ice surface can significantly increase the solar flux to the upper ocean surface (Perovich, Light, et al., 2007). Low-albedo ponds replace the highly reflective, highly attenuating surface scattering layer atop pond-free sea ice, reducing the aggregate albedo of ice-covered areas, and increas-

ing absorption within the sea ice itself (Frey, Perovich, & Light, 2011; Langleben, 1969; Nicolaus, Katlein, Maslanik, & Hendricks, 2012). Arctic surface melt onset has trended towards earlier months in recent decades (Schröder, Feltham, Flocco, & Tsamados, 2014; Stroeve, Markus, Boisvert, Miller, & Barrett, 2014), closer to the peak of the annual solar energy cycle, and is a main driver of increasing solar energy input to the Arctic Ocean (Perovich, Light, et al., 2007). Locally, enhanced solar radiation below newly-formed ponds can enhance sea ice basal melting and further increase solar heating of the upper ocean (Fetterer & Untersteiner, 1998; Perovich, Nghiem, Markus, & Schweiger, 2007). This heat is of critical importance for understanding the seasonal and inter-annual evolution of the sea ice cover (Perovich, Nghiem, et al., 2007). Thinner, more readily ponded first-year ice can transmit much more solar radiation to the upper ocean than multi-year ice (Nicolaus et al., 2012).

At the scale of the ponds themselves, the inhomogeneous transmission of solar energy through through ponded sea ice surfaces leads to an inhomogenous under-ice light field (Katlein, Nicolaus, & Petrich, 2014; Katlein, Perovich, & Nicolaus, 2016). Such inhomogeneity is not resolved in climate models, which instead average it over a grid cell within each model time step, equivalent to a rapid horizontal mixing process in the surface ocean (Holland, 2003; Losch, Herlufsen, & Timmermann, 2006). Vertical mixing close to the ice base, however, can be more rapid than this implied lateral mixing (McPhee, 1992; MCPhee & Morison, 2001), and may be inappropriately accounted for in ocean-sea-ice models (Barthélemy, Fichefet, Goosse, & Madec, 2016). Observations of the under-ice light field in the presence of ponds demonstrate local sub-ice solar radiation maxima directly under regions of bare sea ice near ponded areas, a possible consequence of lateral transmission of solar irradiance by scattering of the light field through the sea ice (Frey et al., 2011; Katlein et al., 2014, 2016). We will consider the potential consequences of this geometrically-driven variation in the under-ice light field, in situations where horizontal mixing or transport is weak compared to vertical mixing and heat delivery to the ice base.

Solar radiation is also the primary energy source for phytoplankton. Arctic phytoplankton blooms are often observed at the ice edge following sea ice retreat (Perrette, Yool, Quartly, & Popova, 2011). Changes to the sea ice surface are likely responsible for an increase in blooms occurring earlier in the melt season and under the ice, away from the ice edge (Arrigo et al., 2012, 2014; Assmy et al., 2017; Horvat et al., 2017; Mundy

et al., 2009). Measurements of atmospheric iodine in a Greenland ice core may be explained by a significant increase in the fraction of phytoplankton blooms occurring under sea ice in past decades (Cuevas et al., 2018).

Observational and modeling studies have thus far investigated the transmission and absorption of solar radiation through ponded, bare, first-year, and mixed regions of sea ice (Laney, Krishfield, & Toole, 2017; Laney et al., 2014; Light, Grenfell, & Perovich, 2008; Light, Perovich, Webster, Polashenski, & Dadic, 2015; Lu, Li, Zhang, & Dong, 2008; Nicolaus et al., 2012; Taskjelle, Hudson, Granskog, & Hamre, 2017), and relationships between sensor geometry and the 3-D light field under simple regions of mixed water, ice, and ponds (Katlein et al., 2016). Here we will investigate the statistical relationship between the under-ice light field and variations in the pond surface geometry, under a fixed region of thin, ponded, first-year sea ice. In Section 2, we describe a method for generating synthetic pond geometries atop sea ice and model the three-dimensional light field under these surfaces. We then examine the statistical features of the under-ice-light field for a synthetic dataset of 5,000 ponded ice surfaces, and demonstrate that the partitioning of solar energy is determined by metrics related to the overlying pond geometry in Section 3. We explore how pond geometry affects under-ice primary production and sea ice evolution in Section 4.1.

2 Methods

2.1 Generation of synthetic pond surfaces

We use synthetic pond surfaces to investigate the statistics of the under-ice light field, allowing us to generate a large number of pond surface configurations with controlled statistical properties. The code to produce these pond surfaces and perform all computations in this study is publicly available as a github repository (Supporting Data). In the first stage of pond generation, a surface is created by imposing a uniform lattice of individual circular “pseudo-ponds” of radius r^* and a total pond fraction ϕ^* , together defining a spacing between successive pond centers, $L^2 \approx \pi(r^*)^2/\phi^*$. In the second stage, the positions and radii of individual ponds are perturbed by white noise with a magnitude equal to $2r^*$ and $2L$, respectively. Through this perturbation procedure, the initially circular and separate ponds overlap and form non-circular floe networks with a total surface pond fraction $\phi \neq \phi^*$.

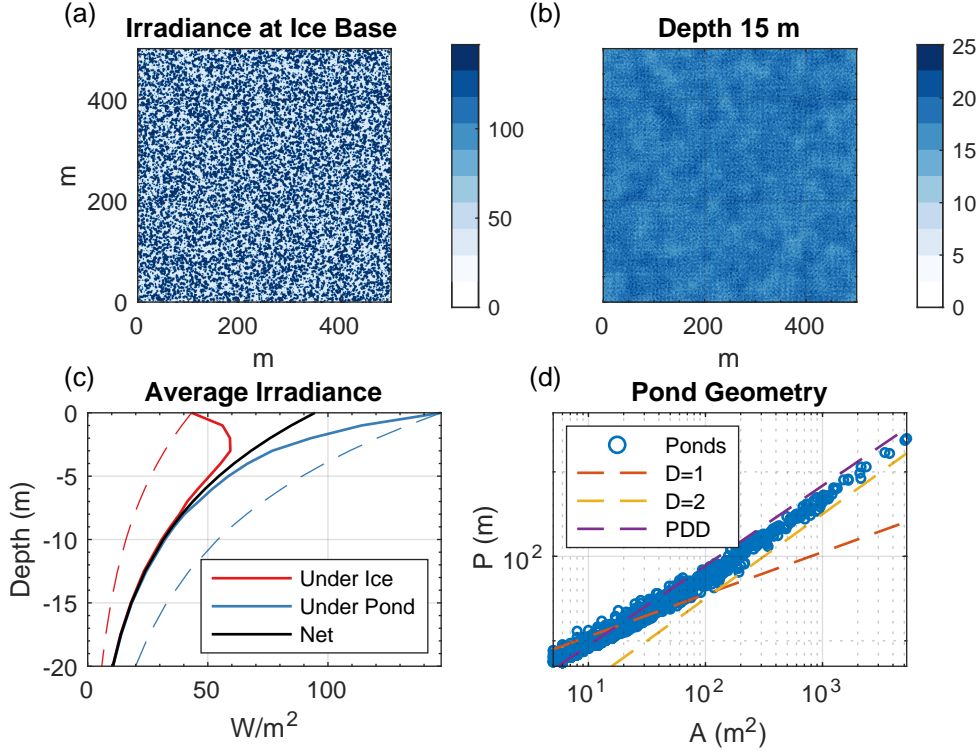


Figure 1. Statistics of a light field under a synthetically generated ponded ice surface. (a) Downwelling planar irradiance (W/m^2) at the ice-ocean interface. (b) Downwelling planar irradiance 15 meters below the ice-ocean interface. Note the changed color scale from (a) to (b). (c) Downwelling planar irradiance as a function of depth for (blue) unponded regions, (red) ponded regions, and (black) all. Dashed lines indicate the expected decay profile for a homogenous surface of all ponds or no ponds. (d) Relationship between pond perimeter and pond area for all connected ponds in (a) (blue circles), with slopes corresponding to a fractal dimension of 1 (red dashed line), 2 (yellow dashed line), or the PDD=1.5 (purple dashed line). The “pond distribution dimension” (PDD) is discussed in Section 2.3.

Fig. 1a shows a synthetic ponded sea ice layer using $r^* = 1$ m and $\phi^* = 0.3$, with a pond fraction $\phi = 0.52$. The ice layer is 1 meter thick, subject to a solar forcing of 350 W/m^2 . The surface is 500 meters square at a resolution of 1 meter (dark blue areas are ponded, white areas are unponded). Values are the downwelling planar irradiance at the ice-ocean interface.

For each synthetically generated ponded surface, we use an edge-detection algorithm to identify all individual (non-circular) ponds that are formed through the per-

turbation procedure above. Indexing the collection of ponds with i , each has a perimeter P_i and area A_i . Across all ponds in an image, the relationship between pond perimeter and area scales with a fractal dimension, D_i , according to,

$$P_i \propto (\sqrt{A_i})^{D_i}. \quad (1)$$

We plot the relationship between perimeter and area for all individual ponds as blue circles in Fig. 1d, and note that an estimate of the fractal dimension of ponds of a certain size is twice the local slope of the $(\log P_i, \log A_i)$ scatter plot in Fig. 1d. A statistical method for obtaining a best fit function $D(A)$ for the dependence of pond fractal dimension D on pond area A for a collection of data $(\log P_i, \log A_i)$ is obtained in Bowen, Strong, and Golden (2018). Observations of ponded sea ice display a transition in $D(A)$ from $D = 1$ to about $D = 2$ as pond area increases, with the transitional regime centered around 100 m^2 (Hohenegger et al., 2012; Huang, Lu, Lei, Xie, & Li, 2016). Dashed lines in Fig. 1d show the slopes corresponding to $D = 1$ (red) and $D = 2$ (yellow), and reproduce the observed transition regime, with results consistent with other methods of pond surface generation (Bowen et al., 2018; Ma, Sudakov, Strong, & Golden, 2019; Popović, Cael, Silber, & Abbot, 2018). Thus our method of pond generation is geometrically realistic.

2.2 Under-ice light field calculation

The solar irradiance at the ice-ocean interface $I_{i/p}$ (units W/m^2 , with the subscript i corresponding to bare ice, and p to ponded ice) is assumed to follow,

$$I_{i/p} = SW I_{0,i/p} (1 - \alpha_{p/i}) \exp(-\kappa_{i/p} H). \quad (2)$$

We take $SW = 350 \text{ W}/\text{m}^2$ to be a representative downwelling solar heat flux in the July Arctic (Kanamitsu et al., 2002; Vihma, 2014). The albedo of the sea ice surface varies in time as it melts because of its surface scattering layer (C. Grenfell & Maykut, 1977). We choose representative values of $\alpha_i = 0.7$, $\alpha_p = 0.25$, $\kappa_i = 1$, and $\kappa_p = 0.7 \text{ m}^{-1}$, $H = 1\text{m}$, $I_{0,p} = .75$, and $I_{0,i} = 0.4$ for, respectively, the albedo of bare ice, the albedo of ponded ice, the extinction coefficient of bare ice, the extinction coefficient of ponded ice, and the thickness of first-year sea ice, the fraction of solar irradiance penetrating the surface scattering layer of ponded ice, and the fraction of solar irradiance penetrating the surface scattering layer of bare melting ice (T. Grenfell, Light, & Perovich, 2006; Light et al., 2008).

In this idealized model of light transmission through sea ice we assume ponds have a constant pond depth. Changes in ice/pond thickness or surface albedos affect the magnitude of solar radiation penetrating the ice. In this study, we focus on the horizontal variability in the light field. Variations in the magnitude of the solar radiation penetrating sea ice are accounted for in Delta-Eddington parameterizations of light transfer in climate models (Briegleb & Light, 2007; Holland, Bailey, Briegleb, Light, & Hunke, 2012; Lenoble, 1985). In the Supplementary Fig. S1 we perform a sensitivity experiment that assumes no surface scattering layer ($I_{0,i} = I_{0,p} = 1$) and the same extinction coefficient under ice and ponds ($\kappa_i = \kappa_p = 0.7 \text{ m}^{-1}$), finding similar results.

We calculate the three-dimensional under-ice light field using the Katlein et al. (2016) ray-optical radiative transfer model, which calculates the downwelling planar irradiance in the ocean below sea ice. The downwelling solar plan irradiance is transmitted as described in Katlein et al. (2014). For a given point in the ocean, we compute the downwelling planar irradiance by integrating over all rays reaching that point from the surface, assuming no scattering within the ocean and that light is attenuated following Beer's law with an extinction coefficient of $\kappa_w = 0.11 \text{ m}^{-1}$. We perform this calculation for each point in the ocean to arrive at the full under-ice field, and assume a doubly-periodic domain so that there are no edge effects.

Fig. 1c shows statistics of the under-ice light field for the pond surface in Fig. 1a. The average planar irradiance (Fig. 1c, black line) decays exponentially with a decay length scale $\kappa_w^{-1} = 9 \text{ m}$, yet as a consequence of the inhomogenous distribution of light penetrating sea ice, the average planar irradiance under ponded ice (Fig. 1c, blue line) or pond-free ice (Fig. 1c, red line) does not follow an exponential decay profile (dashed lines, Fig. 1c). Instead, the initially heterogeneous light field becomes more homogeneous at depth (Fig. 1b). In pond-free areas, there is a significant increase in solar irradiance up to a depth of several meters (Frey et al., 2011).

For the melt pond surface shown in Fig. 1a with a pond area fraction, $\phi = 0.52$, a domain-wide average of 100 W/m^2 of solar energy penetrates the sea ice base, with 70 W/m^2 absorbed in the top 10 meters. Per square meter of sea-ice surface, most of that solar energy (80 W/m^2) penetrates ponded areas, versus 20 W/m^2 through bare ice. If there was no horizontal redistribution of solar energy with depth, the absorption of solar radiation would also be partitioned between ponded and unponded regions at

the same proportion. Instead, an average of 55 W/m² is absorbed in ocean points below melt ponds, and 45 W/m² is absorbed at ocean points below bare ice. In the case of Fig. 1a, when taking into account the effect of pond geometry, the radiation absorbed in the upper ocean under bare ice is more than doubled.

2.3 Fractal geometry and the pond distribution dimension

We next define a fractal-geometrical parameter that we call the “pond distribution dimension” (PDD) to characterize how melt water is distributed over the sea ice surface. In fractal geometry, the box-counting dimension, D_{bc} , is derived from the relationship between the number of boxes, n_i , of side length R_i , that are necessary to cover the perimeter of a fractal region. Under the standard scaling assumption $n_i \sim R_i^{-D_{bc}}$ as $i \rightarrow \infty$, the box counting dimension is defined as,

$$D_{bc} = - \lim_{i \rightarrow \infty} \frac{\log n_i}{\log R_i}. \quad (3)$$

An approximant to the box-counting dimension at each scale indexed by i can be defined,

$$D_{bc,i} = - \frac{\Delta \log n_i}{\Delta \log R_i}, \quad (4)$$

where $\Delta \log n_i = \log n_{i+1} - \log n_i$ and similarly for $\Delta \log R_i$. For a discretized fractal pond surface, $D_{bc,i}$ would be nearly constant for small i . However, pond surfaces do not exhibit scale invariance, so $D_{bc,i}$ is not constant.

We define the PDD as the average value of $D_{bc,i}$, weighted by the number of boxes of radius i ,

$$\text{PDD} = \frac{1}{\mathcal{N}} \sum_i n_i D_{bc,i} = \langle D_{bc,i} \rangle. \quad (5)$$

where $\mathcal{N} = \sum n_i$. This weighting emphasizes coverings by smaller box sizes (small i).

Note that if $D_{bc,i}$ is constant, then $\text{PDD} = D_{bc}$.

While similar in form to traditional measures of two-dimensional geometry Farmer (1982), the newly defined PDD is distinct in that it is generally anti-correlated with increasing connectivity (Fig. 3a-c) and attains values less than 1 for isolated small ponds (Fig. 2). In Supplementary Fig. S2 we show the PDD is poorly correlated with pond area, perimeter, box-counting dimension, or Hausdorff dimension. However, Supplementary Fig. S3a shows that the PDD is related to the fraction of ponds that have a small area.

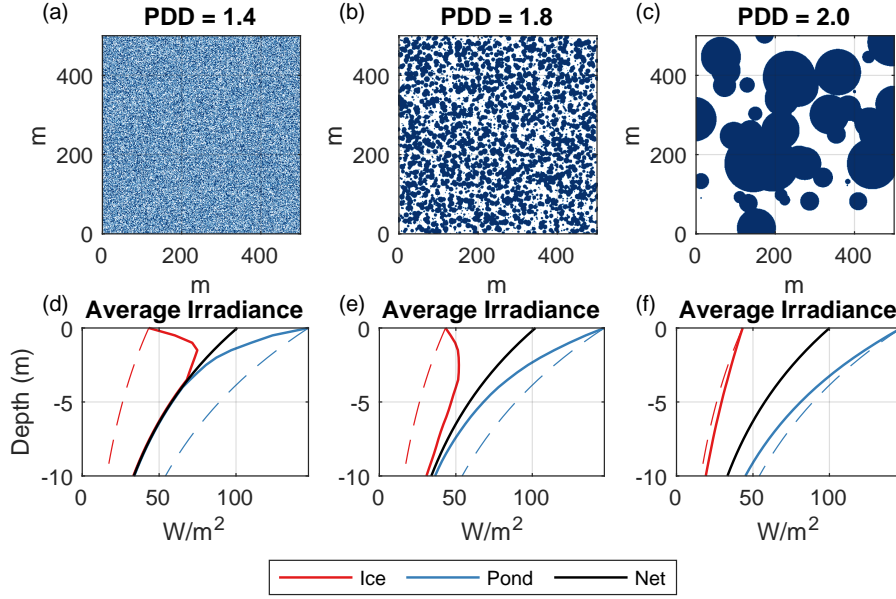


Figure 2. (a-c) Pond surfaces with melt pond fraction $\phi = 0.5$, with variable pond distribution dimension (PDD) of (a) 1.38, (b) 1.76, or (c) 1.96. Blue regions are ponded, white are unpounded. (d-f) Average irradiance as a function of depth under bare ice (red), ponded ice (blue), or all ice regions (black) for the pond surfaces in (a-c). Dashed lines are the average irradiances under each surface type if the surface had only ponds (blue) or bare ice (red).

3 Results

We generate 5,000 square synthetic pond surfaces (as described in 2), each 500×500 square meters and characterized by a PDD obtained by varying r^* between 1 and 500 and ϕ^* between 0 and 1 (see supplementary data D1 for the surfaces and light statistics). Fig. 2(a-c) shows three example pond surfaces each with a melt pond fraction $\phi = 0.5$, for which the PDD ranges from 1.4 to 2. Fig. 2(d-f) show the average light field under all ponded (blue) or all unpounded regions for the surfaces in Fig. 2(a-c).

If solar irradiance propagated straight downwards, the “predicted” solar flux to a region of ocean beneath ponded or bare ice is,

$$I_{pred,p/i} = I_0(1 - \alpha_{p/i}) \exp(-\kappa_i h_i). \quad (6)$$

To capture the full effect on the column integrated solar energy flux, we define two “enhancement factors”, $E_{p/i}$, equal to the percent change in solar absorption under ponded

or pond-free regions relative to this predicted exponential decay,

$$E_{p/i} = \frac{I_{abs,p/i} - I_{pred,p/i}}{I_{pred,p/i}}, \quad (7)$$

where $I_{abs,p/i}$ is the total solar absorption in ocean columns under ponds or bare ice, and $I_{pred,ic}$ is the absorption in those regions assuming exponential extinction and no radial distribution of solar irradiance. A significant percentage of penetrating solar radiation is absorbed in pond-free regions, with the solar flux in these regions increased by 50% or more. Fig. 3c shows the total change in heat flux absorbed in the ponded or unponded regions. Typical values of the heat flux, Q_{trans} , exchanged between ponded and unponded regions are up to 15 W/m².

To determine quantitatively what controls the (negative) enhancement factor for ponded regions, we perform a multiple linear regression of E_p against three control variables: the pond fraction ϕ , the pond perimeter per area non-dimensionalized by the attenuation coefficient, $\frac{P}{\kappa_w A}$ (where A is the total domain area), and PDD. The full regression accounts for nearly all the variance in E_p ($R^2 = .993$),

$$\tilde{E}_p = \left(-0.62 + .29\text{PDD} + 0.04\phi - 6 \times 10^{-3} \frac{P}{\kappa_w A} \right) \approx -0.6 + 0.3\text{PDD}. \quad (8)$$

Regressing on PDD alone compares favorably ($R^2 = 0.988$) to the full multi-linear regression. Because E_p is measured as a percentage change in irradiance, the weak relationship between E_p and ϕ is expected, as ϕ controls the magnitude of solar input. The weaker relationship between the (dimensionless) total pond perimeter per ice area $P/\kappa_w A$ and E_p is more surprising. In Supplementary Fig. S2 we show perimeter-based metrics are weakly associated with E_p compared to PDD. In Supplementary Fig. 3b we show a potentially useful relationship between PDD and the fraction of ponds that have a small area, a metric that may be easier to observe than the PDD.

Inhomogeneous and anisotropic radiative transfer through sea ice affects the horizontal distribution of solar energy with depth, but it does not alter the domain-averaged downward solar flux at each depth, which follows Beer's law (see Fig. 2(d-f)). Thus a relationship between the enhancement factor, E_i , for pond-free regions (red circles, Fig. 3b) and PDD may be derived. Considering the partitioning of total solar energy as it decays with depth between under-ice and under-pond regions,

$$E_i = -E_p \frac{I_{pred,mp}}{I_{pred,ic}}. \quad (9)$$

Noting that in our model of light transmission through ice:

$$\frac{I_{pred,p}}{I_{pred,ic}} = \frac{(1 - \alpha_p)(\phi)}{(1 - \alpha_i)(1 - \phi)}, \quad (10)$$

we derive an expression for E_i ,

$$E_i = -E_p \frac{\phi}{1 - \phi} \frac{1 - \alpha_p}{1 - \alpha_i}. \quad (11)$$

Owing to the reciprocal in Eq. 11, the linear regression model fails when including values of ϕ approaching 1. Restricting to just the values of ϕ smaller than 0.7 (85% of the dataset, and accounting for almost all field observations), the linear model for E_i explains most of the variance in E_i ($R^2 = 0.975$). For clarity, the linear model for E_i is not shown in Fig. 3b, as the fit is no longer a one-to-one function of PDD. A multiple linear regression E_i on the same variables used to derive Eq. 8 returns a model that explains less of the variance ($R^2 = 0.75$) than the nonlinear model of Eq. 11. We are therefore confident the relation of Eq. 11 is appropriate, given the nearly linear scatter plot of E_p in Fig. 3b.

We now derive a model for Q_{trans} , the energy transferred from ponded to unponded regions because of scattering at the ice-ocean interface,

$$\tilde{Q}_{trans}(\phi, \text{PDD}) = I_0 e^{-\kappa_i h} \phi (1 - \alpha_p) \tilde{E}_p \approx I_0 e^{-\kappa_i h} \phi (1 - \alpha_p) (0.3 \text{PDD} - 0.6). \quad (12)$$

This model explains 89% of the variance in the value of Q_{trans} derived by integrating the explicitly computed light field (Fig. 3c).

In summary, we determined a nearly linear relationship between E_p and PDD (Fig. 3b), suggesting the changing absorption of heat is controlled by weighted moments of the pond geometry. In Supplementary Fig. S4, we show the linear relationship is robust, though its slope is affected by the dimensionless quantity $\kappa_w \Delta x$, the attenuation coefficient of light in water multiplied by the minimum pond spacing Δx . Pond geometry affects the transfer of energy between ponded and unponded regions, and a larger value of PDD typically corresponds to well-separated ponds (Fig. 2c), where the transfer of energy is small and hence the enhancement factor is close to zero. A smaller value of PDD (Fig. 2a) corresponds to more connected geometry, more transfer of energy away from ponded regions and hence a more negative enhancement factor E_p . From this linear fit we derive models $\tilde{E}_p(\text{PDD})$ and $\tilde{E}_i(\text{PDD}, \phi)$ that explain 97% and 98% of the variance in E_i and E_p , respectively (Fig. 3b, black line), and a model for the heat flux, \tilde{Q}_{trans} that explains 89% of the variance in Q_{trans} as a function of melt pond fraction and PDD.

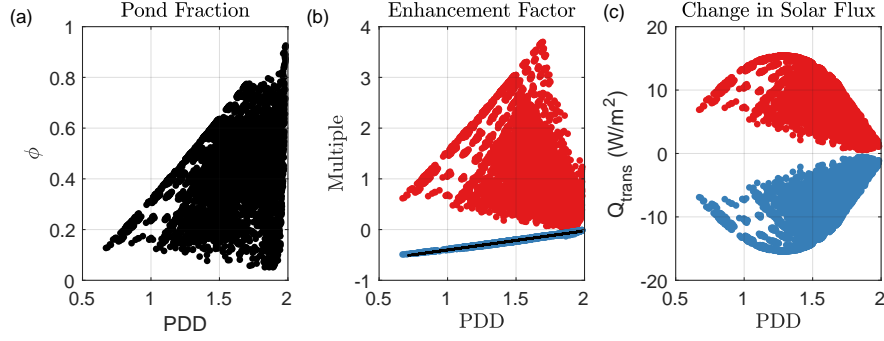


Figure 3. Relationship between under-ice light field and pond geometry for a collection of 5,000 stochastically generated melt pond surfaces. (a) Scatter plot of PDD against melt pond fraction, ϕ . (b) The “enhancement factor”, $E_{p,i}$ in solar absorption for regions under ponds (blue circles) or bare ice (red). The black line is a linear model (Eq. 8) for E_p as a function of PDD. (c) The absolute change in solar heating Q_{trans} under ponded regions (blue) or pond-free regions (red), as a function of PDD.

4 Implications

4.1 Implications for phytoplankton blooms under sea ice

A common framework for understanding phytoplankton blooms is the “Sverdrup hypothesis” (Sverdrup, 1953), which theorizes that phytoplankton inhabit and are evenly mixed throughout the ocean surface mixed layer. When the mixed layer depth is shallower than a “critical depth,” the average photosynthetically available radiation permits phytoplankton community growth, and leads to blooms. Observations of “massive” phytoplankton blooms under fully ice-covered areas of the Chukchi Sea (Arrigo et al., 2012, 2014) have suggested that melt ponds are the main source of the required solar radiation.

Fig. 4a uses the Sverdrup critical depth model for phytoplankton blooms under ponded sea ice derived in Horvat et al. (2017) to examine how changes to the pond surface geometry affect the potential for phytoplankton blooms. To do so, we assume sea ice is static and the differences between ponded and un-ponded regions remain fixed over the time for net primary production to begin. This may be contrasted with the approach in Horvat et al. (2017), which assumed a horizontally homogenized light field over the scale of a single GCM grid cell. The critical depth is the deepest possible mixed layer that al-

lows for net primary production. For purely homogeneous surfaces, ocean areas under ponds (dashed blue line) permit blooms for mixed layers up to 101 meters deep, and ocean areas under bare ice (dashed red line) permit blooms when the mixed layer is 5 meters or less. In general, higher critical depths correspond to better light conditions for photosynthetic life.

The under-ice light field homogenizes with increasing PDD. As PDD decreases, there is a linear decrease in irradiance under ponded regions (blue dots, Fig. 2b), with less photosynthetically available radiation there. Ponded regions therefore become less hospitable, with the critical depth decreasing significantly, to as low as 57 meters. Conversely, this leads to more hospitable conditions under bare ice, and the critical depth in those regions increases by a factor of up to 10 times as a function of PDD (red dots, Fig. 4a).

4.2 Implications for ocean heat fluxes to Arctic sea ice

Pond geometry may also feed back on sea-ice evolution through the ocean heat flux. We test the significance of this mechanism by parameterizing it in a standalone Arctic sea ice simulation. We use the CICE 5.1 sea ice model (Hunke, Lipscomb, Turner, Jeffery, & Elliott, 2015) forced by the JRA55 atmospheric reanalysis over the period 1975–2015. In each grid cell CICE uses a prognostic melt pond model that carries meltwater as a tracer atop “level” regions of sea ice (Flocco, Schroeder, Feltham, & Hunke, 2012). Each grid cell contains a sea ice thickness distribution, with each thickness category of thickness h_j having an ice area fraction, c_j , a melt pond fraction ϕ_j , and a snow fraction s_j .

CICE evaluates two shortwave penetrative heat fluxes in each thickness category: the heat flux per square meter of ponded ice $I_{p,j}^0$, and the heat flux per square meter of unponded ice $I_{i,j}^0$, with,

$$I_p^0 = \sum_j c_j \phi_j I_{p,j}^0, \quad I_i^0 = \sum_j c_j (1 - \phi_j) I_{i,j}^0, \quad (13)$$

where the total sea ice concentration c and melt pond fraction ϕ are obtained via,

$$c = \sum_i c_i; \quad \phi = \sum_i c_i \phi_i. \quad (14)$$

As CICE does not include information about melt pond geometry, we build a linear model for the “enhancement factor”, E_p , as a function of melt pond fraction, ϕ ,

$$E_p(\phi) = -\frac{1 - \phi}{4}. \quad (15)$$

This model does not fit the relationship between E_p and ϕ , though it captures the broad behavior of E_p , ranging from zero decrease in the shortwave heating under ponded ice to a reduction of 25%. We apply a correction factor to the penetrative shortwave in the slab ocean model,

$$I_p = (1 + E_p)I_p^0, \quad (16)$$

$$I_i = (1 + E_i)I_i^0 = \left(1 - E_p \frac{I_p^0}{I_i^0}\right) I_i^0. \quad (17)$$

This corrective factor is applied in each thickness category. The slab ocean model integrates all penetrative shortwave fluxes. Therefore the increase in solar heating under bare ice, and the decrease under ponded ice are applied directly to the base of sea ice. By definition, there is no net change to the energy budget of a single model grid cell, only a redistribution because of these geometric effects of solar energy between ponded and pond-free regions.

Fig. 4b shows the impact of including this redistribution of heat on the simulated September thickness of Arctic sea ice. As changes to geometric properties of the sea ice surface alone do not change the total heat budget of ocean or ice, changes to the modeled sea ice between runs with or without this parameterization derive instead from a feedback on the sea ice thickness distribution. The feedback results in modest changes of ± 2.5 cm in the Arctic basin. Along the Canadian archipelago, where simulated sea ice is thickest, the variability reaches up to 1 meter in localized areas. Overall, these calculations suggest that the feedback process is relatively weak.

5 Conclusions

Here we have demonstrated the significant role that pond surface geometry can have on the light field under sea ice. We found a metric, the pond distribution dimension (PDD), that can be derived from the 2-D pond surface geometry and captures the horizontal partitioning of under-ice irradiance.

Photosynthetic life under ice depends on the availability of light transmitted through the pond-and-ice surface. The two-dimensional geometry of melt ponds partitions solar radiation between ponded and unponded regions as a function of the pond distribution dimension. For regimes with little intra-pond spacing, this redistribution may help support photosynthetic life under bare ice. Pond geometry may also limit the availabil-

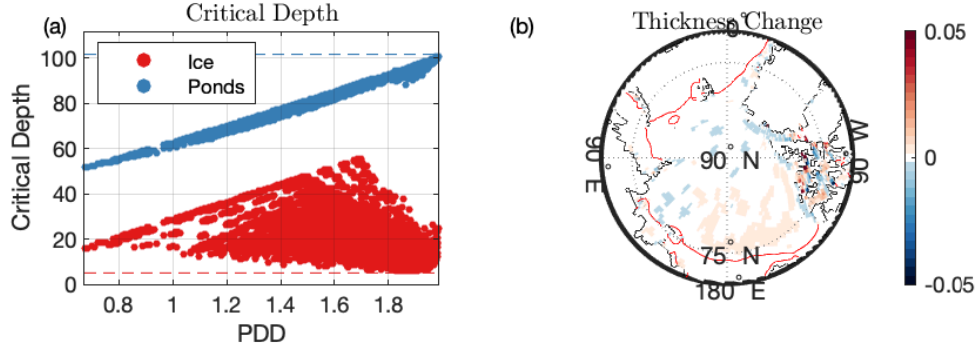


Figure 4. Impacts of surface inhomogeneity under ponded ice. (a) Critical depth under ponded (red) and unponded (blue) surfaces) as a function of pond distribution dimension. Dashed lines are the critical depth for those regions when scattering at the ice-ocean interface is not included. (b) Difference in September Arctic mean sea ice thickness between CICE simulations with or without an idealized sub-gridscale parameterization of under-pond to under-bare-ice energy transfer. Red line is the 15% sea ice concentration contour.

ity of solar radiation under ponds, potentially delaying the onset of blooms otherwise predicted using bulk models of light transmission through ice.

We considered the instantaneous light field under ponded sea ice surfaces. When interpreted as a heat flux, the variation in solar absorption under ponded and bare-ice regions is also instantaneous. However, many ecological communities experience a delay between solar energy absorption and net primary production Lewis et al. (2019). Primary production is also nonlinearly related to solar energy input and other local factors (Boyd et al., 2013). The effect of surface geometry is likely important in regions with weak horizontal ocean mixing or weak relative motion between ice and ocean, or mobile phytoplankton populations that inhabit preferred areas under bare or ponded ice. Scattering of light within the water column was not a focus of our study, but can play a significant role in the distribution of solar energy with depth.

We demonstrated a relationship between a pond distribution dimension (PDD) and solar radiation partitioning, though the PDD cannot readily be derived in current climate models. Here we use synthetically generated ponds and can readily compute statistics of the ponded surface. Obtaining the same for real ponded ice surfaces and ice topographies will be an observational challenge. A first step may be to re-process existing observations of melt ponds over sea ice (Hohenegger et al., 2012) to derive a seasonal

cycle of PDD. Information about the real-world evolution of PDD during the melt season may help to fully understand the impact of melt ponds on Arctic climate, sea ice, and ecology.

Acknowledgments

CH was supported by the NOAA Climate and Global Change Postdoctoral Fellowship Program, sponsored in part through cooperative agreement number NA16NWS4620043, Years 2017–2021, with the National Oceanic and Atmospheric Administration, U.S. Department of Commerce. K.M.G. acknowledges support from the the Applied and Computational Analysis Program and the Arctic and Global Prediction Program at the US Office of Naval Research through grants N00014-13-10291, N00014-15-1-2455, N00014-18-1-2041, and N00014-18-1-2552, as well as support from the Division of Mathematical Sciences and the Division of Polar Programs at the U.S. National Science Foundation through Grants DMS-0940249, DMS-1413454, and DMS-1715680. LR was supported by Marsden contract VUW1408 and the Deep South National Science Challenge. The generated synthetic pond surfaces used to produce the results, along with statistics of their light fields, are included as Supplementary Data.

References

- Arrigo, K. R., Perovich, D. K., Pickart, R. S., Brown, Z. W., van Dijken, G. L., Lowry, K. E., ... Swift, J. H. (2012, jun). Massive Phytoplankton Blooms Under Arctic Sea Ice. *Science*, 336(6087), 1408. doi: 10.1126/science.1215065
- Arrigo, K. R., Perovich, D. K., Pickart, R. S., Brown, Z. W., van Dijken, G. L., Lowry, K. E., ... Swift, J. H. (2014, jul). Phytoplankton blooms beneath the sea ice in the Chukchi sea. *Deep-Sea Research Part II: Topical Studies in Oceanography*, 105, 1–16. doi: 10.1016/j.dsr2.2014.03.018
- Assmy, P., Fernández-Méndez, M., Duarte, P., Meyer, A., Randelhoff, A., Mundy, C. J., ... Granskog, M. A. (2017, dec). Leads in Arctic pack ice enable early phytoplankton blooms below snow-covered sea ice. *Scientific Reports*, 7(1), 40850. doi: 10.1038/srep40850
- Barthélemy, A., Fichet, T., Goosse, H., & Madec, G. (2016, aug). A multi-column vertical mixing scheme to parameterize the heterogeneity of oceanic conditions under sea ice. *Ocean Modelling*, 104, 28–44. doi: 10.1016/

- 390 j.ocemod.2016.05.005
- 391 Bowen, B., Strong, C., & Golden, K. M. (2018). Modeling the fractal geometry of
 392 Arctic melt ponds using the level sets of random surfaces. *Journal of Fractal
 393 Geometry*, 5(2).
- 394 Boyd, P. W., Rynearson, T. A., Armstrong, E. A., Fu, F., Hayashi, K., Hu,
 395 Z., ... Thomas, M. K. (2013, may). Marine Phytoplankton Tempera-
 396 ture versus Growth Responses from Polar to Tropical Waters Outcome
 397 of a Scientific Community-Wide Study. *PLoS ONE*, 8(5), e63091. doi:
 398 10.1371/journal.pone.0063091
- 399 Briegleb, B. P., & Light, B. (2007). *A Delta-Eddington multiple scattering pa-
 400 rameterization for solar radiation in the sea ice component of the Community
 401 Climate System Model* (Vol. NCAR/TN-47; Tech. Rep. No. February). Na-
 402 tional Center for Atmospheric Research. Technical Note TN-472STR, Na-
 403 tional Center for Atmospheric Research, Boulder, CO, United States. doi:
 404 10.5065/D6B27S71
- 405 Cuevas, C. A., Maffezzoli, N., Corella, J. P., Spolaor, A., Vallelonga, P., Kjær, H. A.,
 406 ... Saiz-Lopez, A. (2018). Rapid increase in atmospheric iodine levels in the
 407 North Atlantic since the mid-20th century. *Nature Communications*, 9(1),
 408 1452. doi: 10.1038/s41467-018-03756-1
- 409 Farmer, J. D. (1982, jan). Information Dimension and the Probabilistic Structure of
 410 Chaos. *Zeitschrift für Naturforschung A*, 37(11), 1304–1326. doi: 10.1515/zna-
 411 -1982-1117
- 412 Fetterer, F., & Untersteiner, N. (1998). Observations of melt ponds on Arctic sea
 413 ice. *Journal of Geophysical Research: Oceans*, 103(C11), 24821–24835. doi: 10
 414 .1029/98JC02034
- 415 Flocco, D., Schroeder, D., Feltham, D. L., & Hunke, E. C. (2012). Impact of melt
 416 ponds on Arctic sea ice simulations from 1990 to 2007. *Journal of Geophysical
 417 Research: Oceans*, 117(9), 1–17. doi: 10.1029/2012JC008195
- 418 Frey, K. E., Perovich, D. K., & Light, B. (2011). The spatial distribution of solar
 419 radiation under a melting Arctic sea ice cover. *Geophysical Research Letters*,
 420 38(22), L22501. doi: 10.1029/2011GL049421
- 421 Grenfell, C., & Maykut, G. A. (1977). The optical properties of ice and snow in the
 422 Arctic Basin. *J. Glaciol.*, 18(80), 445–463. doi: 10.1017/S0022143000021122

- Grenfell, T., Light, B., & Perovich, D. K. (2006). Spectral transmission and implications for the partitioning of shortwave radiation in arctic sea ice. *Annals of Glaciology*, 44, 1–6.
- Hohenegger, C., Alali, B., Steffen, K. R., Perovich, D. K., & Golden, K. M. (2012). Transition in the fractal geometry of Arctic melt ponds. *Cryosphere*, 6(5), 1157–1162. doi: 10.5194/tc-6-1157-2012
- Holland, M. M. (2003). An improved single-column model representation of ocean mixing associated with summertime leads: Results from a SHEBA case study. *Journal of Geophysical Research*, 108(C4), 3107. doi: 10.1029/2002JC001557
- Holland, M. M., Bailey, D. A., Briegleb, B. P., Light, B., & Hunke, E. (2012). Improved sea ice shortwave radiation physics in CCSM4: The impact of melt ponds and aerosols on Arctic sea ice. *Journal of Climate*, 25(5), 1413–1430. doi: 10.1175/JCLI-D-11-00078.1
- Horvat, C., Jones, D. R., Iams, S., Schroeder, D., Flocco, D., & Feltham, D. (2017, mar). The frequency and extent of sub-ice phytoplankton blooms in the Arctic Ocean. *Science Advances*, 3(3), e1601191. doi: 10.1126/sciadv.1601191
- Huang, W., Lu, P., Lei, R., Xie, H., & Li, Z. (2016). Melt pond distribution and geometry in high Arctic sea ice derived from aerial investigations. *Annals of Glaciology*, 57(73), 105–118. doi: 10.1017/aog.2016.30
- Hunke, E. C., Lipscomb, W. H., Turner, A. K., Jeffery, N., & Elliott, S. (2015). *CICE : the Los Alamos Sea Ice Model Documentation and Software User’s Manual Version 5.1 LA-CC-06-012* (Tech. Rep.). Los Alamos National Laboratory.
- Kanamitsu, M., Ebisuzaki, W., Woollen, J., Yang, S. K., Hnilo, J. J., Fiorino, M., & Potter, G. L. (2002, nov). NCEP-DOE AMIP-II reanalysis (R-2). *Bulletin of the American Meteorological Society*, 83(11), 1631–1643+1559. doi: 10.1175/BAMS-83-11-1631(2002)083<1631:NAR>2.3.CO;2
- Katlein, C., Nicolaus, M., & Petrich, C. (2014). The anisotropic scattering coefficient of sea ice. *Journal of Geophysical Research: Oceans*, 119(2), 842–855. doi: 10.1002/2013JC009502
- Katlein, C., Perovich, D. K., & Nicolaus, M. (2016). Geometric Effects of an Inhomogeneous Sea Ice Cover on the under Ice Light Field. *Frontiers in Earth Science*, 4(February), 2–11. doi: 10.3389/feart.2016.00006

- 456 Laney, S. R., Krishfield, R. A., & Toole, J. M. (2017). The euphotic zone under
457 Arctic Ocean sea ice: Vertical extents and seasonal trends. *Limnology and*
458 *Oceanography*, 62(5), 1910–1934. doi: 10.1002/lno.10543
- 459 Laney, S. R., Krishfield, R. A., Toole, J. M., Hammar, T. R., Ashjian, C. J., &
460 Timmermans, M.-L. (2014, jun). Assessing algal biomass and bio-optical dis-
461 tributions in perennially ice-covered polar ocean ecosystems. *Polar Science*,
462 8(2), 73–85. doi: 10.1016/j.polar.2013.12.003
- 463 Langleben, M. P. (1969, jan). Albedo and Degree of Puddling of a Melting
464 Cover of Sea Ice. *Journal of Glaciology*, 8(54), 407–412. doi: 10.1017/
465 S002214300002699X
- 466 Lenoble, J. (1985). Radiative Transfer in Scattering and Absorbing Atmospheres:
467 Standard Computational Procedures. *Hampton, VA, A. Deepak Publishing*,
468 1985, 314 p..
- 469 Lewis, K. M., Arntsen, A. E., Coupel, P., Joy-Warren, H., Lowry, K. E., Matsuoka,
470 A., ... Arrigo, K. R. (2019, jan). Photoacclimation of Arctic Ocean phyto-
471 plankton to shifting light and nutrient limitation. *Limnology and Oceanogra-*
472 *phy*, 64(1), 284–301. doi: 10.1002/lno.11039
- 473 Light, B., Grenfell, T. C., & Perovich, D. K. (2008, mar). Transmission and ab-
474 sorption of solar radiation by Arctic sea ice during the melt season. *Journal of*
475 *Geophysical Research: Oceans*, 113(3), C03023. doi: 10.1029/2006JC003977
- 476 Light, B., Perovich, D. K., Webster, M. A., Polashenski, C., & Dadic, R. (2015,
477 nov). Optical properties of melting first-year Arctic sea ice. *Journal of Geo-*
478 *physical Research: Oceans*, 120(11), 7657–7675. doi: 10.1002/2015JC011163
- 479 Losch, M., Herlufsen, S., & Timmermann, R. (2006). Effects of heterogeneous sur-
480 face boundary conditions on parameterized oceanic deep convection. *Ocean*
481 *Modelling*, 13(2), 156–165. doi: 10.1016/j.ocemod.2005.12.003
- 482 Lu, P., Li, Z. J., Zhang, Z. H., & Dong, X. L. (2008, feb). Aerial observa-
483 tions of floe size distribution in the marginal ice zone of summer Prydz
484 Bay. *Journal of Geophysical Research: Oceans*, 113(C2), n/a—n/a. doi:
485 10.1029/2006JC003965
- 486 Ma, Y.-P., Sudakov, I., Strong, C., & Golden, K. M. (2019, jun). Ising model for
487 melt ponds on Arctic sea ice. *New Journal of Physics*, 21(6), 063029. doi: 10
488 .1088/1367-2630/ab26db

- 489 McPhee, M. G. (1992). Turbulent heat flux in the upper ocean under sea ice. *Jour-*
 490 *nal of Geophysical Research*, 97(C4), 5365. doi: 10.1029/92JC00239
- 491 McPhee, M. G., & Morison, J. H. (2001). Under-ice Boundary Layer. In *Encyclope-*
 492 *dia of ocean sciences* (pp. 3071–3078). Elsevier. doi: 10.1006/rwos.2001.0146
- 493 Mundy, C. J., Gosselin, M., Ehn, J., Gratton, Y., Rossnagel, A., Barber, D. G., ...
 494 Papakyriakou, T. (2009). Contribution of under-ice primary production to
 495 an ice-edge upwelling phytoplankton bloom in the Canadian Beaufort Sea.
 496 *Geophysical Research Letters*, 36(17), L17601. doi: 10.1029/2009GL038837
- 497 Nicolaus, M., Katlein, C., Maslanik, J., & Hendricks, S. (2012, dec). Changes in Arc-
 498 tic sea ice result in increasing light transmittance and absorption. *Geophysical*
 499 *Research Letters*, 39(24), 2012GL053738. doi: 10.1029/2012GL053738
- 500 Perovich, D. K., Light, B., Eicken, H., Jones, K. F., Runciman, K., & Nghiem,
 501 S. V. (2007). Increasing solar heating of the Arctic Ocean and adjacent seas,
 502 19792005: Attribution and role in the ice-albedo feedback. *Geophysical Re-*
 503 *search Letters*, 34(19), L19505. doi: 10.1029/2007GL031480
- 504 Perovich, D. K., Nghiem, S. V., Markus, T., & Schweiger, A. (2007, mar). Sea-
 505 sonal evolution and interannual variability of the local solar energy absorbed
 506 by the Arctic sea iceocean system. *Journal of Geophysical Research*, 112(C3),
 507 C03005. doi: 10.1029/2006JC003558
- 508 Perovich, D. K., & Richter-Menge, J. a. (2009, jan). Loss of Sea Ice in the Arctic.
 509 *Annual Review of Marine Science*, 1(1), 417–441. doi: 10.1146/annurev.marine
 510 .010908.163805
- 511 Perrette, M., Yool, A., Quartly, G. D., & Popova, E. E. (2011, feb). Near-ubiquity
 512 of ice-edge blooms in the Arctic. *Biogeosciences*, 8(2), 515–524. doi: 10.5194/
 513 bg-8-515-2011
- 514 Polashenski, C., Golden, K. M., Perovich, D. K., Skvillingstad, E., Arnsten, A.,
 515 Stwertka, C., & Wright, N. (2017, jan). Percolation blockage: A process that
 516 enables melt pond formation on first year Arctic sea ice. *Journal of Geophysi-*
 517 *cal Research: Oceans*, 122(1), 413–440. doi: 10.1002/2016JC011994
- 518 Polashenski, C., Perovich, D., & Courville, Z. (2012). The mechanisms of sea ice
 519 melt pond formation and evolution. *Journal of Geophysical Research: Oceans*,
 520 117(1). doi: 10.1029/2011JC007231
- 521 Popović, P., Cael, B. B., Silber, M., & Abbot, D. S. (2018, apr). Simple Rules

- 522 Govern the Patterns of Arctic Sea Ice Melt Ponds. *Physical Review Letters*,
523 120(14), 148701. doi: 10.1103/PhysRevLett.120.148701
- 524 Rösel, A., Kaleschke, L., & Birnbaum, G. (2012). Melt ponds on Arctic sea ice
525 determined from MODIS satellite data using an artificial neural network. *The*
526 *Cryosphere*, 6(2), 431–446. doi: 10.5194/tc-6-431-2012
- 527 Schröder, D., Feltham, D. L., Flocco, D., & Tsamados, M. (2014, may). Septem-
528 ber Arctic sea-ice minimum predicted by spring melt-pond fraction. *Nature*
529 *Climate Change*, 4(5), 353–357. doi: 10.1038/nclimate2203
- 530 Stroeve, J. C., Markus, T., Boisvert, L., Miller, J., & Barrett, A. (2014, feb).
531 Changes in Arctic melt season and implications for sea ice loss. *Geophysi-*
532 *cal Research Letters*, 41(4), 1216–1225. doi: 10.1002/2013GL058951
- 533 Sverdrup, H. U. (1953, jan). On Conditions for the Vernal Blooming of Phytoplank-
534 ton. *ICES Journal of Marine Science*, 18(3), 287–295. doi: 10.1093/icesjms/
535 18.3.287
- 536 Taskjelle, T., Hudson, S. R., Granskog, M. A., & Hamre, B. (2017, sep). Modelling
537 radiative transfer through ponded first-year Arctic sea ice with a plane-parallel
538 model. *Cryosphere*, 11(5), 2137–2148. doi: 10.5194/tc-11-2137-2017
- 539 Vihma, T. (2014). Effects of Arctic Sea Ice Decline on Weather and Climate: A Re-
540 view. *Surveys in Geophysics*, 35(5), 1175–1214. doi: 10.1007/s10712-014-9284
541 -0